Dalton Transactions

Responsive Fluorinated Nanoemulsions for ^{19}F Magnetic Resonance Detection of Cellular Hypoxia

Journal:	*Dalton Transactions*
Manuscript ID	DT-ART-03-2020-001182.R1
Article Type:	Paper
Date Submitted by the Author:	08-Jul-2020
Complete List of Authors:	Kadakia, Rahul; University of Texas at Austin, Chemistry Xie, Da; University of Texas at Austin, Chemistry Guo, Hongyu; University of Texas at Austin, Department of Chemistry Bouley, Bailey; University of Texas at Austin, Chemistry Yu, Meng; University of Texas at Austin, Chemistry Que, Emily; University of Texas at Austin, Chemistry

ARTICLE

Responsive Fluorinated Nanoemulsions for ^{19}F Magnetic Resonance Detection of Cellular Hypoxia†

Received 00th January 20xx,
Accepted 00th January 20xx

DOI: 10.1039/x0xx00000x

Rahul T. Kadakia,‡ Da Xie,‡ Hongyu Guo, Bailey Bouley, Meng Yu, Emily L. Que*

We report two highly fluorinated Cu-based imaging agents, **CuL$_1$** and **CuL$_2$**, for detecting cellular hypoxia as nanoemulsion formulations. Both complexes retained their initial quenched ^{19}F MR signals due to paramagnetic Cu^{2+}; however, both complexes displayed a large signal increase when the complex was reduced. DLS studies showed that the **CuL$_1$** nanoemulsion (**NE CuL$_1$**) had a hydrodiameter of approximately 100 nm and that it was stable for four weeks post-preparation. Hypoxic cells incubated with **NE CuL$_1$** showed that 40% of the Cu^{2+} uptaken was reduced in low oxygen environments.

Introduction

Hypoxia in solid tumor cancers results from inadequate O_2 delivery to these rapidly dividing cells, resulting in O_2 deficiency. This leads to increased levels of hypoxia inducible factor (HIF-1), which regulates the cells ability to adapt to the new environment.[1, 2] If left untreated, the cells can become resistant to chemotherapy and cause malignant proliferation.[3-6] Therefore, early diagnosis of hypoxic cancer cells is vital for tumor excision to avoid metastasis and secondary malignant tumor growths. An additional effect of hypoxia is a more reducing intracellular environment, which can be used for selective targeting of therapeutic and diagnostic agents. Among the imaging agents that have been developed to target hypoxia,[7-14] ^{64}CuATSM (ATSM = diacetyl-bis(*N*^{4}-methylthiosemicarbazone)) has been used as a positron emission tomography (PET) agent that functions via reduction of the Cu^{2+} complex and retention in hypoxic cells, however this agent requires the use of radioactive materials.[15, 16]

Magnetic resonance imaging (MRI) is the most widely used imaging modality to diagnose cancer and can be used to image whole organisms with high depth penetration without employing ionizing radiation. However, early tumor detection is difficult as the spatial and contrast resolution between cancerous growths and surrounding normal tissue is poor. As an emerging alternative, ^{19}F MRI can be used as there is no detectable fluorine in the body and, thus, any signal present will originate from exogenous agents. Moreover, the ^{19}F nucleus provides comparable characteristics: 100% isotopic abundancy, nuclear spin of ½, 83% MR signal receptivity compared to ^{1}H, and further, the carbon-fluorine bond is biostable.[17]

Previously, we have demonstrated the use of fluorinated CuATSM imaging agents as "turn-on" probes for cellular hypoxia.[7-9] These agents use paramagnetic Cu^{2+}, which serves as a powerful paramagnetic relaxation enhancement (PRE) source that attenuates ^{19}F MR signal due to T_2 shortening.[7-9, 17-21] Following reduction to Cu^+ in hypoxic cells and subsequent demetallation, the ^{19}F signal is fully restored, furnishing a signal turn-on in this environment. For these agents to be a viable option for *in vivo* studies, the need for elevated fluorine concentration on individual probes increases, to allow an overall brighter MRI signal. Unfortunately, the hydrophobic CuATSM scaffold and fluorine atoms decrease aqueous solubility. Therefore, synthesizing a highly fluorinated CuATSM complex also requires a new delivery formulation: nanoemulsions.

Nanoemulsions are nano-sized liquid particles that consist of an oil droplet core, which assists in the dissolution of hydrophobic molecules, and a layer of emulsifier, which is necessary to reduce excess interfacial energy and prevent aggregation (Figure 1).[22, 23] Common emulsifiers are amphiphilic molecules such as phospholipids and pegylated molecules.[24] Importantly, a number of

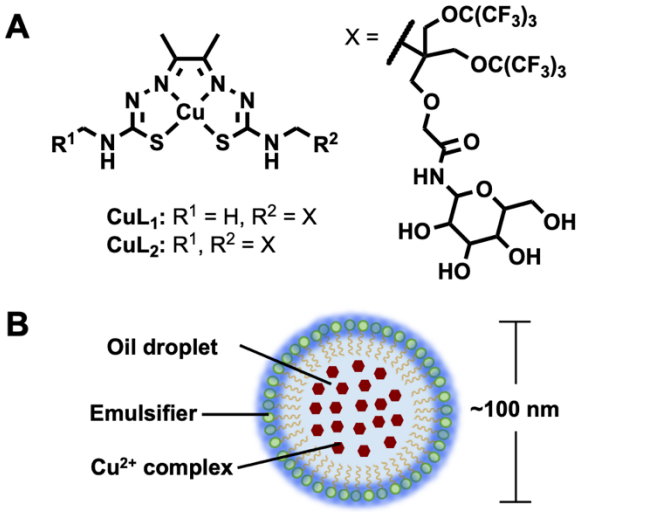

Figure 1. (A) Chemical structures for **CuL$_1$** and **CuL$_2$**. (B) Oil-in-water- nanoemulsion composition.

Department of Chemistry, The University of Texas at Austin, 105 E 24th St Stop A5300, Austin, TX 78712, USA. Email: emilyque@cm.utexas.edu

‡ Contributed equally

† Electronic Supplementary Information (ESI) available. CCDC 1993045. For ESI and CCDC, see DOI: 10.1039/x0xx00000x

^{19}F MRI nanoemulsion formulations have been employed to deliver perfluorinated carbon-based agents for *in vivo* imaging.[25-29] By encapsulating the prepared Cu^{2+}-based probes into nanoemulsions, we envisioned that the complexes would maintain high fluorine spin density while staying miscible within the aqueous environment. Herein, we present two CuATSM-derived complexes, **CuL_1** and **CuL_2** (Figure 1), with 18 and 36 equivalent fluorines, respectively. The **CuL_1** complex forms stable nanoemulsions that display "turn-on" in ^{19}F MR modalities upon reduction, and preferential signal turn-on in hypoxic cells.

Results and discussion

Structural characterization

CuL_1 and **CuL_2** incorporate multiple perfluoro-*tert*-butyl units to confer high fluorine density and a glucosamine moiety to tune the overall lipophilicity of the whole complex. Their syntheses are described in full in the Supporting Information. Single crystals of **CuL_1** were grown by evaporation of a concentrated ethanol solution at room temperature and brown, needle-like crystals were collected. The X-ray structure (Figure S1) confirmed a square-planar Cu^{2+} center embedded in the [N_2S_2] pocket, similar to the parent CuATSM complex.[30] Interestingly, hydrogen bonds were observed between two different glucosamine motifs within the crystal packing. The average distance between Cu^{2+} and ^{19}F nuclei was measured as 8.4 Å, a distance at which Cu^{2+} would attenuate the ^{19}F MR signal.[17] Single crystals of **CuL_2** did not form.

Solution state characterization

^{19}F NMR characterization. To characterize the effect of Cu^{2+} on the ^{19}F NMR signal in our complexes, we obtained spectra and measured relaxation times of **H_2L_1**, **CuL_1**, **H_2L_2**, and **CuL_2**. The ^{19}F NMR spectra (Figure S2) of **CuL_1** and **CuL_2** demonstrated that Cu^{2+} broadens the ^{19}F signal in these complexes as compared to their respective ligands **H_2L_1** and **H_2L_2**. The relaxation times (Table 1) of the fluorine atoms decreased by roughly 30-fold for T_1 and 100-fold for T_2. The larger fold of decrease in T_2 is consistent with the longer electronic relaxation time T_{1e} of the square planar Cu^{2+} center.[31, 32] The singlet peak observed for all prepared ligands and complexes indicated that the fluorine atoms are all magnetically equivalent, which is a benefit for maximizing the signal-to-noise ratio (SNR) in ^{19}F MR-based sensing.

Table 1 - ^{19}F NMR parameters for 3 mM **H_2L_1**, **CuL_1**, **H_2L_2**, and **CuL_2** in d_6-DMSO at room temperature at 9.4 T. [a] Due to the fast transverse relaxation for **CuL_1** and **CuL_2**, the T_2 was too short to be measured.

	H_2L_1	**CuL_1**	**H_2L_2**	**CuL_2**
δ (ppm)	-70.0	-69.9	-70.0	-70.0
T_1 (ms)	590	20.4	675	22.2
T_2 (ms)	360	N/A[a]	333	N/A[a]
T_2* (ms)	157	4.3	78.2	2.2

Cyclic voltammetry. To understand the redox properties of **CuL_1** and **CuL_2**, the Cu^{2+}/Cu^{+} redox potentials were determined by cyclic voltammetry in DMF (Figure S3). Measured half potentials of -0.62 V for **CuL_1** and -0.60 V for **CuL_2** were close to the reported values for the parent CuATSM complex (-0.63 V vs. SCE), revealing the potential for these complexes to target hypoxic cells.[33] Due to the presence of the quaternary carbon, the electron-withdrawing perfluoro-*tert*-butoxide and glucosamine moiety did not significantly change the reduction potential of the Cu^{2+} centers. This observation also indicates other R groups (instead of glucosamine) could be incorporated into this molecular scaffold to further functionalize or solubilize the complex. The ΔE_p values of **CuL_1** and **CuL_2** indicate that the reduction of **CuL_1** is quasi-reversible while the reduction of **CuL_2** is irreversible. Considering the different coordination preferences between Cu^{+} and Cu^{2+}, the large bulkiness of the functional groups on **H_2L_2** could result in a lower stability for [**$Cu^{+}L_2$**] than [**$Cu^{+}L_1$**], thus making the reduction process for **CuL_2** less reversible than **CuL_1**.

Preparation of nanoemulsion

Formulation. To improve incorporation of these complexes into aqueous media, an oil-in-water nanoemulsion formulation strategy was employed. **H_2L_1**, **CuL_1**, **H_2L_2**, and **CuL_2** nanoemulsions (namely, **NE H_2L_1**, **NE CuL_1**, **NE H_2L_2**, and **NE CuL_2**) were prepared following published literature.[26] Lecithin, Milli-Q water, and safflower oil were mixed and heated at 80 °C to form the emulsion mixture. **H_2L_1**, **CuL_1**, **H_2L_2**, and **CuL_2** were dissolved in DMSO and the hot, pre-made emulsion was added directly to the DMSO solution, vortexed to create a crude emulsion, and ultrasonicated at 0 °C to afford a stock nanoemulsion (Scheme S2). Unfortunately, upon reduction of **NE CuL_2** with $Na_2S_2O_4$, both **NE CuL_2** and the reduced **NE CuL_2** gave similar T_2* values and chemical shifts, making them difficult to differentiate under MR settings. Therefore, all future studies were performed with **NE CuL_1**.

Size determination. The size distribution of **NE CuL_1** was evaluated by dynamic light scattering (DLS). In water and various buffered environments, **NE CuL_1** displayed a hydrodynamic diameter of ~100 nm with PDI ≤ 0.20 (Table 2). These results are consistent with reported results on similar systems[34, 35] and suggest effective formation of the nanoemulsion formulation. Transmission electronic microscopy (TEM) was employed to visualize the morphology of the prepared **NE CuL_1**, using neutral ammonium phosphomolybdate staining to improve contrast.[23] Therefore, as shown in Figure 2, the nanoemulsions appeared as bright sphere-like structures with a size distribution of 81 ± 19 nm, well correlated with DLS results. Energy-Dispersive X-ray Spectroscopy (EDS) of a single nanoemulsion revealed an even inner distribution of copper and sulfur elements, further confirming the successful preparation of a nanoemulsion containing the **CuL_1** complex.

Table 2 – Size distribution of **NE CuL$_1$** in water and different buffers determined by dynamic light scattering (DLS).

Solvent/Buffer	Average Size (nm)	PDI
Water	93.3 ± 0.7	0.20
PBS	94.5 ± 0.3	0.18
HEPES	97.9 ± 0.2	0.20
RPMI (w/o FBS)	98.0 ± 0.4	0.19
DMEM (w/o FBS)	105.7 ± 0.8	0.16

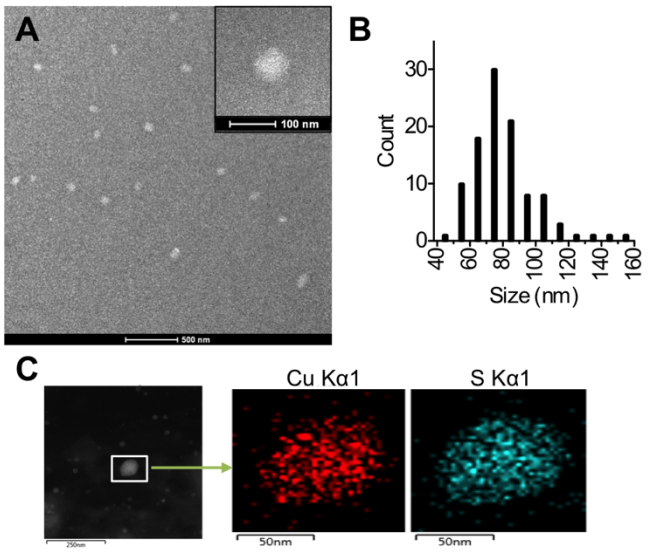

Figure 2. (A) Representative TEM image of **NE CuL$_1$** negatively stained with neutral ammonium phosphomolybdate. Inset: Expanded view of a single nanoemulsion. (B) Size distribution of **NE CuL$_1$** (n=104). (C) Copper and sulfur elemental profiling of a single **NE CuL$_1$** particle by Energy-Dispersive X-ray Spectroscopy (EDS).

Nanoemulsion stability. The stability of both ligand and complex nanoemulsions was assessed by DLS (size) and ^{19}F NMR (fluorine content). The stability of the **NE CuL$_1$** was also assessed by inductively coupled plasma-optical emission spectroscopy (ICP-OES) to evaluate the copper content within the nanoemulsion. As shown in Figure S4, at 100 μM [Cu^{2+}], the prepared **NE CuL$_1$** displayed great aqueous stability with marginal change (< 5%) in both its average size and the polydispersity index (PDI). However, at 5 mM [Cu^{2+}], the **NE CuL$_1$** is prone to aggregation and showed an increase in its average hydrodynamic diameter and a decrease in PDI. Interestingly, although the size distribution of 5 mM **NE CuL$_1$** changed over the course of 28 days, the copper leaching was minimal (< 5%), similar to the 100 μM **NE CuL$_1$**. Additionally, a 100 μM sample of the **NE H$_2$L$_1$** was subjected to DLS and ^{19}F NMR analysis over the course of four weeks after preparation. Compared to the **NE CuL$_1$**, the leaching of **H$_2$L$_1$** within **NE H$_2$L$_1$** was much faster when studied by ^{19}F NMR, especially at a higher ligand concentration (Figure S5). While the 0.5 mM **NE H$_2$L$_1$** showed 6% leaching after two weeks, the 5 mM **NE H$_2$L$_1$** leaching increased to 20% during the same time. The increased cargo leaching for **NE H$_2$L$_1$**, as compared to **NE CuL$_1$**, is likely due to a more polar nature of **H$_2$L$_1$** that encouraged its escape from the nanoemulsion.

Relaxation time determination. To understand the MR properties of **CuL$_1$** and **H$_2$L$_1$** within their nanoemulsion

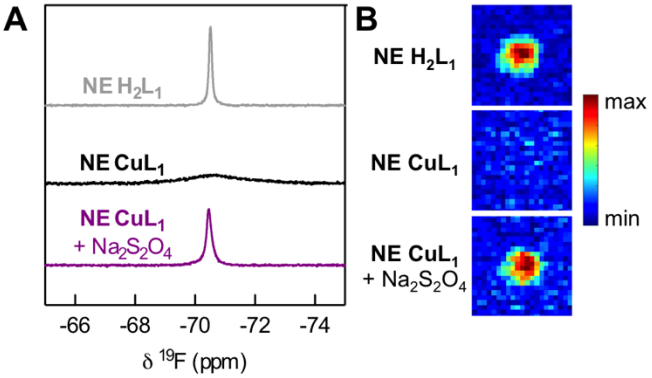

Figure 3. (A) ^{19}F NMR spectra of 1.0 mM **NE H$_2$L$_1$**, **NE CuL$_1$**, and reduced **NE CuL$_1$**. (B) Phantom ^{19}F MRI of 1.0 mM **NE H$_2$L$_1$**, **NE CuL$_1$**, and reduced **NE CuL$_1$**.

environments, ^{19}F NMR spectra were taken for each nanoemulsion (Figure 3A). **NE H$_2$L$_1$** displayed an intense singlet peak at -70.5 ppm. On the other hand, **NE CuL$_1$** gave a very broad peak at -70.7 ppm. Fluorine relaxation times (T_1 and T_2) were measured for both nanoemulsions (Table 3). **NE H$_2$L$_1$** had a T_1 of 380 ms and a T_2 of 7.0 ms, which was much shorter compared to that of the DMSO solution of **H$_2$L$_1$**. The large decrease in T_2 is likely due to the viscous safflower oil core of the nanoemulsion and potential intermolecular aggregation due to hydrogen bonding between the glucose motifs as observed in the crystal packing. The T_1 relaxation time of **NE CuL$_1$** was too short to measure and the T_2^* was 0.4 ms, consistent with its broad and nearly quenched signal.

Table 3 – ^{19}F NMR parameters of 0.5 mM **NE H$_2$L$_1$**, **NE CuL$_1$**, and reduced **NE CuL$_1$** at room temperature. [a] The peak for **NE CuL$_1$** was broad. [b] Due to the fast transverse relaxation for **NE CuL$_1$**, the T_1 and T_2 were too short to be measured.

	NE H$_2$L$_1$	**NE CuL$_1$**	**NE CuL$_1$** + $Na_2S_2O_4$
δ (ppm)	-70.5	-70.7[a]	-70.5
T_1 (ms)	380	N/A[b]	440
T_2 (ms)	7.0	N/A[b]	4.4
T_2* (ms)	7.0	0.4	4.4

Redox behavior. To determine if the chemical reduction of **CuL$_1$** would successfully happen inside the nanoemulsion, 1.0 mM test-tube reactions between $Na_2S_2O_4$ and **NE CuL$_1$** were carried out (Figure 3A). Upon addition of $Na_2S_2O_4$, the characteristic orange-brownish color of **CuL$_1$** disappeared immediately, and the whole nanoemulsion system turned off-white, consistent with reduction of Cu^{2+} to Cu^{+}. The ^{19}F NMR characteristics of the reduced system were similar to the **NE H$_2$L$_1$** (δ = -70.5 ppm; T_1 = 0.44 s; T_2 = 4.4 ms) (Table 3). Therefore, while being encapsulated inside the nanoemulsion, **CuL$_1$** was likely converted to **H$_2$L$_1$** upon reduction. We note that there was no significant change to the ^{19}F NMR of **NE H$_2$L$_1$** in the presence of $Na_2S_2O_4$ (Figure S6).

The reduction of the Cu^{2+} center within the nanoemulsion was further confirmed via UV-vis absorption and EPR spectroscopy (Figures S7). Before reduction, the UV-vis absorption spectrum of **NE CuL$_1$** displayed a characteristic Cu^{2+} d-d absorption peak

at 480 nm[36] and the EPR spectral pattern was well correlated to a square planar Cu^{2+} center[37, 38] with g_{iso} = 2.061 and A_{Cu} = 106 G. Post reduction, all these spectral features were lost, consistent with reduction of Cu^{2+}. Importantly, the UV-vis absorption spectrum of **NE CuL$_1$** was recovered upon exposing the reduced **NE CuL$_1$** to air, indicating that the binding of Cu^{2+} by **H$_2$L$_1$** was not perturbed by the presence of the nanoemulsion formulation.

Phantom MR images. Phantom ^{19}F MR imaging for 1.0 mM **NE H$_2$L$_1$**, **NE CuL$_1$**, and reduced **NE CuL$_1$** were performed. Fast-low-angle-shot (FLASH) pulse sequence was applied to allow tracking of species with short T_2 values. As shown in Figure 3B, Cu^{2+} effectively quenches the ^{19}F MR signal and the signal-to-noise ratio for **NE CuL$_1$** was on the same level as noise (SNR = 2.2). On the other hand, an intense signal was captured for the **NE H$_2$L$_1$** (SNR = 12) and the reduced **NE CuL$_1$** (SNR = 7.6), each with the same ^{19}F concentration as the **NE CuL$_1$**. These results demonstrated a "turn-on" response in the ^{19}F MR imaging modality when **CuL$_1$** is reduced and converted to **H$_2$L$_1$** within nanoemulsion formulations and hold promise for potential ^{19}F MR imaging-based studies.

Cell studies

Cytotoxicity and cell uptake. To evaluate the nanoemulsion's ability to act as a biological probe, cell studies were performed with MCF-7 breast cancer cells. Cytotoxicity of the **NE CuL$_1$** was tested using a Live/Dead assay under both normoxic and hypoxic conditions. Fluorescence imaging data showed >95% viability of the nanoemulsion incubated cells in both normoxic and hypoxic environments (Figure S8). To track the copper content of the MCF-7 cells, cell uptake studies were performed on normoxic and hypoxic cells after 2, 4, and 6-hour incubation (ICP-OES). As shown in Figure S9, a gradual increase in copper uptake was observed for increasing incubation times. At 6 hours, the cellular copper level was 3.2 ± 0.1 fmol/cell, which should give a cellular fluorine content of ~60 fmol/cell. When comparing the copper uptake between normoxic and hypoxic conditions, we saw no differences. This similarity could be due to the fact that **CuL$_1$** was encapsulated in the nanoemulsion and uptake and retention of the nanoemulsion is not dependent on the oxygen level. Uptake studies at 4 °C, a temperature at which energy-dependent active transportation is blocked, showed 9-fold less cellular copper content after 4 hours compared to studies at 37 °C, consistent with an energy-dependent cell uptake pathway. The energy-dependent cell uptake of the **NE CuL$_1$** correlated well with the vesicular character of these formulations.[24]

To visualize the uptake of **NE CuL$_1$**, MCF-7 cells were incubated with a fluorescent ZnSalen complex that has been reported to stain the hydrophobic interior of lipid droplets (Figure 4A).[39] MCF-7 cells were incubated with **NE CuL$_1$** only, with the fluorescent dye only, and with both fluorescent dye and **NE CuL$_1$**, respectively. As expected, no fluorescence was observed within the cells when only **NE CuL$_1$** was administered (Figure 4A top). With incubation of the fluorescent dye itself, cellular fluorescence was weak (Figure 4A middle). When the cells were treated with both **NE CuL$_1$** and the fluorescent dye (Figure 4A bottom), an intense intracellular fluorescence was observed, exhibiting an enhancement of fluorescence by nearly 3-fold

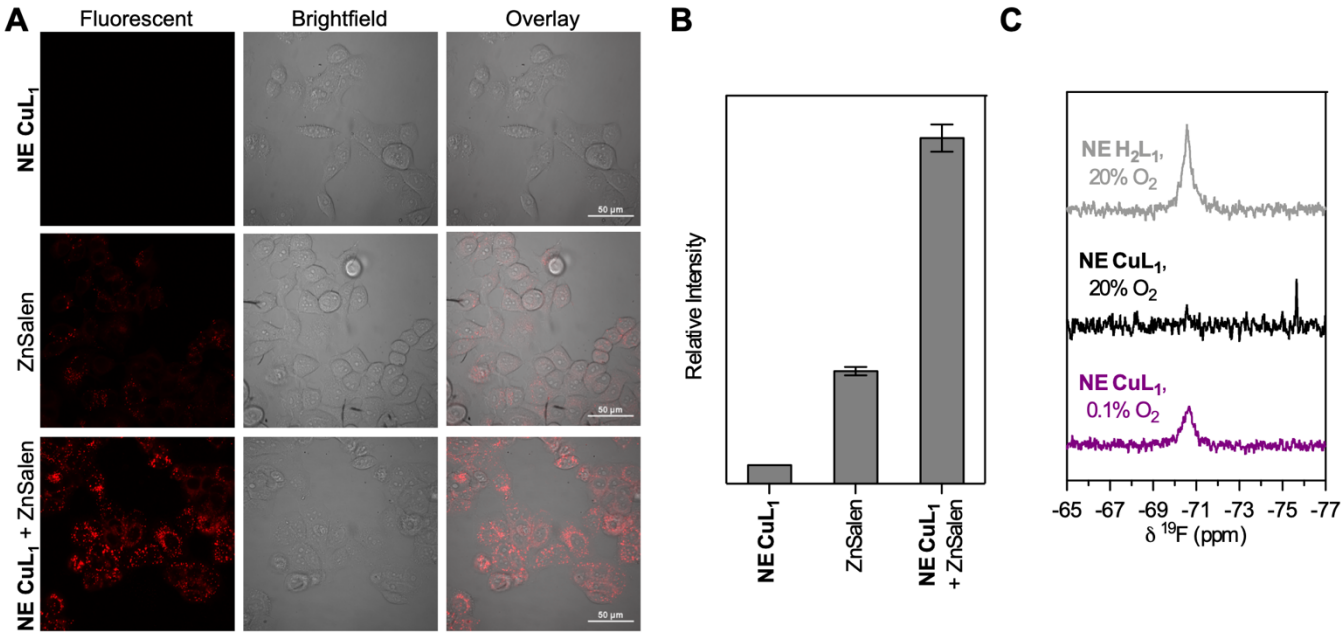

Figure 4. (A) Confocal images of MCF-7 cells incubated with **NE CuL$_1$** (top row), the fluorescent dye (middle row), and both **NE CuL$_1$** and the fluorescent dye (bottom row). (B) Quantitative comparison of intracellular fluorescence of ~100 cells at different incubation conditions. (C) Whole cell ^{19}F NMR of **NE H$_2$L$_1$** (top) and **NE CuL$_1$** (middle) in normoxic (20% O_2) environment and **NE CuL$_1$** (bottom) in hypoxic (0.1% O_2) environment

compared to cells incubated with the fluorescent molecule only (Figure 4B). A closer look at the image revealed dot-like red fluorescence inside the cytoplasm, corresponding to the vesicular character of the nanoemulsions. These results further confirmed efficient uptake of the nanoemulsions into cells.

Cellular hypoxia reduction studies. **NE CuL_1** was employed for hypoxia detection through ^{19}F NMR spectroscopy (Figure 4C). As a positive control, normoxic MCF-7 breast cancer cells were first cultured with 100 μM **NE H_2L_1** for 4 hours. The cells were collected, transferred into an NMR tube, and a ^{19}F NMR spectrum was taken with 5-fluorocytosine (5FC) as external reference. A broad peak was recorded at -70.6 ppm. This result indicated that inside the cytosol, the **NE H_2L_1** stayed intact and its fluorine signal was detectable. Additional MCF-7 cells were incubated with **NE CuL_1** under both normal (20%) and low (0.1%) oxygen tension. Only under the low oxygen tension was a peak at -70.6 ppm observed, indicating the selective reduction of **NE CuL_1** in the cells grown under hypoxic conditions. At 20% O_2, no ligand signal was detected; the trace signal of perfluoro-*tert*-butanol might have come from the slight decomposition of the complex inside the cells. To quantify the cellular reduction of copper inside the cells, the reduced copper content was estimated by ^{19}F NMR spectroscopy (where the peak integration represents the fluorine content of the reduced complex and therefore the amount of copper follows the molar ratio between Cu and F with **CuL_1**, which is 1:18), and the total copper content quantified via ICP-OES. It was therefore determined that roughly 40% of **CuL_1** was reduced in the cytosol under hypoxic conditions.

Conclusions

In summary, we demonstrated a CuATSM-based nanoemulsion sensor system that selectively displays ^{19}F NMR signal in hypoxic cells. CuATSM derivative, **CuL_1**, was embedded within oil-in-water nanoemulsions which displayed ideal morphology and aqueous stability. Switching of the ^{19}F MR signal via tuning of copper redox state was demonstrated by adding chemical reducing agents and the effective reduction of copper was verified by spectroscopic methods. Selective detection of cellular hypoxia was further achieved in breast cancer cells grown under both normoxic (20% O_2) and severe hypoxic (0.1% O_2) conditions, where ~40% of the Cu^{2+} uptaken (~ 1.3 fmol/cell) was estimated to be reduced by cellular machinery. These results thus provide solid evidence that responsive oil-in-water nanoemulsion systems can be used to detect changes in cellular environments using ^{19}F magnetic resonance. Ongoing work includes synthesizing a complex with a larger T_2* and higher cellular uptake for *in vivo* applications.

Conflicts of interest

There are no conflicts to declare.

Acknowledgements

This work was funded by start-up funds from UT-Austin (EQ), a grant from the Welch Foundation (F-1883) (EQ). We thank Dr. Vincent Lynch for X-ray crystallography support. We acknowledge the Biomedical Imaging Center at UT Austin for access to their facilities. Some NMR spectra were obtained on a Bruker AVIII HD 500 that was funded by an NIH grant (J. Sessler, 1 S10 OD021508-01).

References

1. A. E. Greijer and E. van der Wall, *J Clin Pathol*, 2004, **57**, 1009-1014.
2. E. M. Hammond, M. C. Asselin, D. Forster, J. P. O'Connor, J. M. Senra and K. J. Williams, *Clin Oncol (R Coll Radiol)*, 2014, **26**, 277-288.
3. P. Vaupel, A. Mayer and M. Höckel, *Methods Enzymol*, 2004, **381**, 335-354.
4. W. R. Wilson and M. P. Hay, *Nat Rev Cancer*, 2011, **11**, 393-410.
5. A. R. Padhani, K. A. Krohn, J. S. Lewis and M. Alber, *Eur Radiol*, 2007, **17**, 861-872.
6. R. J. Gillies and R. A. Gatenby, *Cancer Metastasis Rev*, 2007, **26**, 311-317.
7. D. Xie, S. Kim, V. Kohli, A. Banerjee, M. Yu, J. S. Enriquez, J. J. Luci and E. L. Que, *Inorg Chem*, 2017, **56**, 6429-6437.
8. D. Xie, T. L. King, A. Banerjee, V. Kohli and E. L. Que, *Journal of the American Chemical Society*, 2016, **138**, 2937-2940.
9. R. T. Kadakia, D. Xie, D. Martinez, M. Yu and E. L. Que, *Chem Commun (Camb)*, 2019, **55**, 8860-8863.
10. J. Pacheco-Torres, P. López-Larrubia, P. Ballesteros and S. Cerdán, *NMR Biomed*, 2011, **24**, 1-16.
11. Q. N. Do, J. S. Ratnakar, Z. Kovács and A. D. Sherry, *ChemMedChem*, 2014, **9**, 1116-1129.
12. S. Takahashi, W. Piao, Y. Matsumura, T. Komatsu, T. Ueno, T. Terai, T. Kamachi, M. Kohno, T. Nagano and K. Hanaoka, *J Am Chem Soc*, 2012, **134**, 19588-19591.
13. D. J. Yang, S. Wallace, A. Cherif, C. Li, M. B. Gretzer, E. E. Kim and D. A. Podoloff, *Radiology*, 1995, **194**, 795-800.
14. E. Lopci, I. Grassi, A. Chiti, C. Nanni, G. Cicoria, L. Toschi, C. Fonti, F. Lodi, S. Mattioli and S. Fanti, *Am J Nucl Med Mol Imaging*, 2014, **4**, 365-384.
15. A. L. Vāvere and J. S. Lewis, *Dalton Trans*, 2007, 4893-4902.
16. J. J. Vaquero and P. Kinahan, *Annu Rev Biomed Eng*, 2015, **17**, 385-414.
17. D. Xie, M. Yu, R. T. Kadakia and E. L. Que, *Acc Chem Res*, 2019.
18. J. S. Enriquez, M. Yu, B. S. Bouley, D. Xie and E. L. Que, *Dalton Trans*, 2018, **47**, 15024-15030.
19. H. Chen, X. Tang, X. Gong, D. Chen, A. Li, C. Sun, H. Lin and J. Gao, *Chem Commun (Camb)*, 2020, **56**, 4106-4109.
20. S. Mizukami, R. Takikawa, F. Sugihara, Y. Hori, H. Tochio, M. Wälchli, M. Shirakawa and K. Kikuchi, *J Am Chem Soc*, 2008, **130**, 794-795.

21. K. H. Chalmers, E. De Luca, N. H. Hogg, A. M. Kenwright, I. Kuprov, D. Parker, M. Botta, J. I. Wilson and A. M. Blamire, *Chemistry*, 2010, **16**, 134-148.
22. Y. Singh, J. G. Meher, K. Raval, F. A. Khan, M. Chaurasia, N. K. Jain and M. K. Chourasia, *Journal of Controlled Release*, 2017, **252**, 28-49.
23. V. Klang, N. B. Matsko, C. Valenta and F. Hofer, *Micron*, 2012, **43**, 85-103.
24. M. Jaiswal, R. Dudhe and P. K. Sharma, *3 Biotech*, 2015, **5**, 123-127.
25. A. A. Kislukhin, H. Xu, S. R. Adams, K. H. Narsinh, R. Y. Tsien and E. T. Ahrens, *Nature Materials*, 2016, **15**, 662.
26. I. Tirotta, A. Mastropietro, C. Cordiglieri, L. Gazzera, F. Baggi, G. Baselli, M. G. Bruzzone, I. Zucca, G. Cavallo, G. Terraneo, F. Baldelli Bombelli, P. Metrangolo and G. Resnati, *Journal of the American Chemical Society*, 2014, **136**, 8524-8527.
27. J. M. Janjic and E. T. Ahrens, *Wiley Interdisciplinary Reviews: Nanomedicine and Nanobiotechnology*, 2009, **1**, 492-501.
28. T. Nakamura, H. Matsushita, F. Sugihara, Y. Yoshioka, S. Mizukami and K. Kikuchi, *Angew Chem Int Ed Engl*, 2015, **54**, 1007-1010.
29. K. Akazawa, F. Sugihara, M. Minoshima, S. Mizukami and K. Kikuchi, *Chem Commun (Camb)*, 2018, **54**, 11785-11788.
30. A. R. Cowley, J. R. Dilworth, P. S. Donnelly, E. Labisbal and A. Sousa, *J Am Chem Soc*, 2002, **124**, 5270-5271.
31. I. Bertini, P. Turano and A. J. Vila, *Chem. Rev.*, 1993, **93**, 2833-2932.
32. I. Bertini, C. Luchinat, G. Parigi and E. Ravera, *NMR of Paramagnetic Molecules*, Elsevier, Boston, 2 edn., 2017.
33. J. L. Dearling, J. S. Lewis, G. E. Mullen, M. J. Welch and P. J. Blower, *J Biol Inorg Chem*, 2002, **7**, 249-259.
34. J. M. Janjic, M. Srinivas, D. K. Kadayakkara and E. T. Ahrens, *J Am Chem Soc*, 2008, **130**, 2832-2841.
35. S. K. Patel, J. Williams and J. M. Janjic, *Biosensors*, 2013, **3**.
36. R. Mukherjee, *Comprehensive Coordination Chemistry II*, Pergamon, Oxford, 2003.
37. J. Peisach and W. E. Blumberg, *Arch Biochem Biophys*, 1974, **165**, 691-708.
38. S. Ushio and A. W. Addison, *J. Chem. Soc., Dalton Trans.*, 1979, 600-608.
39. J. Tang, Y. Zhang, H. Y. Yin, G. Xu and J. L. Zhang, *Chem Asian J*, 2017, **12**, 2533-2538.

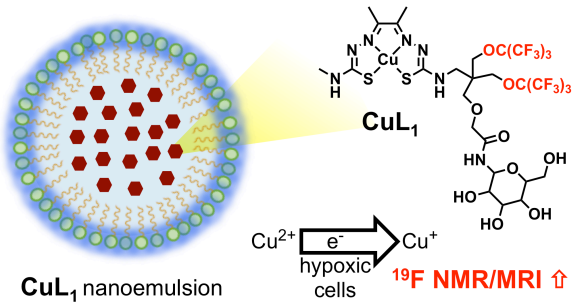

A highly fluorinated Cu^{2+} complex for ^{19}F MR sensing of cellular hypoxia as nanoemulsion formulations.